Correlation of Optical Properties, Electronic Structure and Photocatalytic Activity in Nanostructured Tungsten Oxide

Min Ling, Christopher S. Blackman,[*] Robert G. Palgrave, Carlos Sotelo-Vazquez, Andreas Kafizas and Ivan P. Parkin

Dr. Min Ling, Dr. Christopher S. Blackman, Dr. Carlos Sotelo-Vazquez, Dr. Robert G. Palgrave, Dr Andreas Kafizas, Dr. Ivan P. Parkin, University College London, Department of Chemistry, 20 Gordon St., London WC1H 0AJ (United Kingdom).
E-mail: c.blackman@ucl.ac.uk

Abstract: Tungsten trioxide nanorod arrays were deposited using aerosol assisted chemical vapour deposition. The electronic structure, defect chemistry, optical bandgap and photocatalytic activity were found to vary progressively with nanorod length. Nanorods less than 1 µm in length showed a widening of the optical bandgap (up to 3.1 eV), more disorder states within the bandgap, an absence of reduced tungsten cation states, and increased photocatalytic activity for destruction of a test organic pollutant (stearic acid) compared to nanorods of 2 µm length or greater which possessed bandgaps close to the bulk value for tungsten oxide (2.6 – 2.8 eV), the presence of reduced tungsten states (W^{4+}), and lower photocatalytic activity. The results indicate that for maximum photocatalytic performance in organic pollutant degradation, tungsten oxide should be engineered such that the bandgap is widened relative to bulk WO3 to a value above 3 eV; although less photons are expected be absorbed, increases in the over-potential for oxidation reactions appear to more than offset this loss. It is also desirable to ensure the material remains defect free, or the defect concentration minimised, to minimise carrier recombination.

1. Introduction

The bandgap and band edge positions of metal oxide semiconductors are crucial in photocatalytic applications and heterojunction design. Tungsten oxide possesses a band gap at around 2.6 eV, has valence band maximum (VBM) edge (*vs.* NHE) sufficiently positive to oxidise H_2O producing intermediate hydroxyl ($\cdot$OH) radicals, however the conduction band minimum (CBM) edge (*vs.* NHE) is insufficiently negative to reduce O_2 to superoxide ($O_2\cdot$) and/or hydroperoxy ($HO_2\cdot$) radicals. This results in low photocatalytic activity for degradation of organic pollutants by oxidation with radicals.[1–5]

To enhance the photocatalytic performance, the potential strategies for band structure engineering include alloying, doping, or quantum confinement.[6–8] Recently, an attractive approach introduced oxygen vacancies (V_O) in the lattice of 'black' TiO_2 by hydrogen treatment, narrowing the band gap and enhancing the visible light absorption, boosting the photocatalytic activity.[9,10] However, high concentration of V_O can cause a negative effect on the photocatalytic activity by acting as charge-recombination centres.[9] Therefore, controlling the level of V_O plays an important role in defect engineering. The amount of V_O in tungsten oxide was recently reported to be controlled through air-annealing at various temperatures (300 to 600 °C) and times (0.5 to 8 hours), giving improvements in photocatalytic activity and electrochemical performance.[11]

Recently we have investigated the growth and properties of chemical vapour deposited (CVD) nanostructured tungsten oxide.[12] The appearance of defects in the direction perpendicular to NR growth was the driving force for formation of the 1D structure *via* a planar-defect-driven growth mechanism.[13] Herein, we study the growth of tungsten oxide nanorod (NR) array thin films, their one-dimensional (1D) nanostructure growth mechanism and the variable concentration of V_O, and their influence on the photocatalytic properties of the deposited nanomaterial. We find that as the NR grow, the cross-section increases due to the coalescence of adjacent NRs and a change in the V_O concentration is observed. Hence, the

2

V_O concentration in 1D tungsten oxide deposited *via* aerosol assisted chemical vapour deposition (AACVD) is a function of the deposition time. The photocatalytic activity for degradation of stearic acid (SA) irradiated by UVA light (365 nm) was enhanced in the tungsten oxide NR array thin films with low V_O concentration despite possessing wider band gaps (up to 3.1 eV) compared to arrays with a high concentration of V_O (2.6 eV).

2. Results and Discussion

SEM was used to analyse the morphology of the deposited films, which were all comprised of arrays of NR (**Figure S2 and S3**). The length of the NRs is controlled by the deposition time, as shown *via* side-on SEM (**Figure 1**), with depositions 0.5, 1, 3, 5, 10, 20 or 30 minutes long resulting in 350 ± 50, 500 ± 100, 750 ± 150, 1200 ± 200, 1800 ± 400, 3000 ± 500, 4200 ± 550 nm in length respectively.

Glancing angle XRD showed the as-synthesized samples adopted the monoclinic WO_3 crystal structure (a=7.306, b=7.540, c=7.692 Å and β=90.881°, PDF# 01-072-0677, **Figure 2**). The intensity of the dominant reflection (002) became stronger, and lower intensity peaks emerged, as the length of the NRs became longer.

TEM shows the NRs array grow along the [001] direction with diameter increasing from $75 (\pm 5)$ nm (0.5 min) to $170 (\pm 20)$ nm (30 min), in good agreement with XRD, with an interplanar spacing of $0.38 (\pm 0.01)$ nm corresponding to the (002) plane of WO_3 (**Figure 3a to 3c**). The corresponding Fourier transformation of the HRTEM image (**Figure 3b inset**) shows a streak perpendicular to the [001] direction which can be attributed to planar defects in [010] and/or [100] directions.[14] The formation of these planar defects are expected to prevent NR growth along the [010] and [100] directions in which case the NRs would extrude from the nucleation site growing primarily along the [001] direction, consistent with the preferred orientation observed by XRD.

The optical properties of the films varied with deposition time (**Figure 4a to 4c**), with transmittance generally decreasing and reflectance in the visible region increasing with deposition time. The appearance of a distinct absorbance in the NIR (Transmittance + Reflectance + Absorbance = 100%) at around 1000 nm (1.2 eV) was also observed for samples deposited for 10, 20 and 30 mins. Based on the absorbance spectra, the bandgaps of as-synthesized samples were estimated from Tauc plots giving indirect bandgaps ranging from 2.6 - 3.1 eV (**Figure 4d, 4e and S4**) dependent on deposition time compared to bulk WO_3 with indirect bandgap of 2.62 eV.[15] The sample deposited for 30 mins had a bandgap comparable to bulk WO_3, however samples deposited at shorter times showed a widening of the indirect bandgap (**Figure 4d**). The sample deposited for 30 s with a NR length of 350 nm showed an indirect bandgap of around 3.1 eV, similar to values observed for WO_3 quantum dots 1.4 nm wide.[7] As noted above, samples with longer growth times (10 − 30 mins) possessed an additional optical absorption in the NIR region (~ 1000 nm). This has previously been observed in WO_3 containing V_O,[16] where the presence of V_O create a potential well[17] and the energy of incident light needed to excite excess bound electrons is $2E_p$ (where E_p is the polaron binding energy, also described as the activation energy of polaron-hopping) with maximum absorption at around $4E_p$.[16,18] Based on literature values of a small-polaron ground state at 0.15 to 0.2 eV below the CB minimum (dependent on V_O concentration),[18,19] the energy of maximum NIR absorption would be 0.8 to 1.2 eV (1500 to 1000 nm), close to the measured value (~ 1000 nm, **Figure 4c**).

The origin of the widened bandgap, observed in our WO_3 NR arrays cannot be attributed to a quantum size-confinement effect as the NR cross-section is far larger (between 40 and 170 nm dependent on growth time, **Figure 3a**) than the particle size typically required for a semiconductor to exhibit this effect (typically between 1 to 12 nm).[20] We attribute the observed bandgap widening to the formation of dislocation loops; it has previously been

found that strain fields introduced by the presence of dislocation loops lead to quantum-spatial-confinement (QSC) effects, which in the case of silicon can increase the bandgap energy from between 325 and 750 meV due to the stress formed at the edge of dislocation loops.[7] We observed dislocation loops from HRTEM imaging (**Figure 5a** - yellow highlighted boxes) with diameters between 0.4 and 1.5 nm in the NR nucleates from which the WO_3 NRs grow. This was only found in samples with the widest indirect bandgaps (30 seconds – 5 minutes growth time). After nucleation the NRs grow along the [001] direction without defects (as shown in **Figure 5b and 5c**, and consistent with the (002) preferred orientation observed in XRD patterns) and hence the strain fields from these dislocation loops would relax in the NR growth direction. Therefore, as the NR length increases we expect the QSC effect to decrease and for the indirect bandgap to narrow to a value closer to that of bulk WO_3, as observed.

XPS was used to identify the composition of the tungsten oxide NR arrays as shown in **Figure 6a**. At deposition times up to 3 min, the W 4f peaks appear broad yet symmetrical. The corresponding XPS valence band regions are shown in **Figure 6b and Figure S5**. For reduced WO_{3-x}, electrons partially fill the W 5d orbitals and these are detectable close to the Fermi level (BE = 0 eV).[21] For deposition times up to 3 min, no such W 5d peaks are observed in the XPS VB region (yet are seen for longer deposition times). Based on the absence of a detectable W 5d peak in the valence band, the symmetrical (yet broad) W 4f core line XPS peaks, and the absence of a NIR absorption in the optical spectrum (**Figure 5c**), we conclude that only W^{6+} is present in samples of short deposition time, *i.e.* no W^{4+} or other reduced tungsten states are present within the detection limits of the techniques employed. The broad nature of the XPS W 4f peaks may represent a variety of W^{6+} environments, especially surface states or the presence of greater disorder, which is also suggested by valence band results discussed below. The disorder states may relate to the presence of the

dislocation loops observed in TEM, although the lack of reduced tungsten species requires that these loops comprise both cation and anion vacancies.

At longer deposition times, the XPS W 4f peaks become narrower but asymmetric, with a distinct low binding energy shoulder visible, that increased with deposition time. These are modelled with W^{6+} and W^{4+} components, implying the formation of V_O. The presence of W^{4+} in these samples is corroborated by the presence of a NIR optical absorption due to small polaron hopping and also by the presence of a W 5d peak close to the Fermi level in the valence band XPS region (**Figure 6b**). Deconvolution of the W 4f region showed the relative concentration of W^{4+} increasing up to 8.56% (*i.e.* $WO_{2.91}$) as the deposition time increased. The *d*-band within band gap was previously observed in MoO_{3-x} 2D flakes and black TiO_2 nanoparticles containing reduced cation Mo^{5+} and Ti^{3+} respectively in presence of V_O.[10,22]

The gradient and binding energy of the VBM, relative to the Fermi level, the latter calculated by extrapolating the low binding energy edge of the valence band to the spectra baseline, was dependent on the deposition time. The VBM shifted from 2.8 eV in the sample grown for 30 s to 2.3 eV in the sample grown for 30 mins, *i.e.* as deposition time increases the VBM shifts towards the Fermi level (**Figure 6b**). A schematic of the band structure (Figure 7c) illustrates that the expansion of the indirect E_g (from 2.6 to 3.1 eV) at short deposition times is mainly accounted for by the downward shift of the VBM from 2.3 to 2.8 eV below the Fermi level. In this case, assuming the indirect optical transition is at the fundamental bandgap, the CBM is situated 0.2 - 0.3 eV above the Fermi level for all samples. In addition the spectral VBM becomes much sharper at longer deposition times, whereas for short deposition times the valance band spectrum has a considerable tail into the bandgap. This indicates the presence of a low concentration of filled states, which may be due either to surface states or to disorder states, as found in black-TiO_2.[9,10] However, in contrast to black-

TiO$_2$, these disorder states are of much lower spectral intensity and do not appear to cause optical absorption. This may be due to the lower density of these disorder states.

In summary, two distinct regimes of electronic structure can be discerned in these samples. At short deposition times, no reduced W states are detectable either by valence band or core level XPS, or by optical spectroscopy (**Table 1**). In these samples, as NR length decreases (with lower deposition time) the bandgap widens as compared with bulk WO$_3$, which can be accounted for by a lowering of the VBM compared to the Fermi level with the CBM remaining unchanged (relative to the Fermi level). Also at short deposition times a tail of disorder states is detectable by valence band XPS within the bandgap, which may relate to the dislocation loops observed *via* TEM, but these states do not appear to be optically active. XPS core line indicates greater breadth of the W 4f peaks at shorter deposition times, also suggesting greater disorder or greater prevalence of surface W^{6+} states. At longer deposition times, evidence of reduced W states appear in the core level XPS, valence band XPS and optical spectra (**Table 1**). The band gap narrows towards the bulk value due to a decrease in the separation between the Fermi level and the VBM.

The photocatalytic activity of the samples was evaluated by measuring the photodegradation of SA under UVA irradiation (λ_{max} = 365 nm). The area of peaks at 2958, 2923 and 2853 cm^{-1} (**Figure 7a to 7c and Figure S6**) representing for the C-H bonds of SA obtained from IR spectra reduced as illuminated by UVA light from 0 to 27 hour caused by photocatalytic oxidation (Equation 3). The integrated areas of those peaks are shown in Figure 8d, and then the rate of photocatalytic oxide of SA molecules is estimated by linear regression of initial (40 to 50 %) step (**Figure 7d**) with results presented in **Figure S7** used to obtained the FQE by Equation 4 to determine the photocatalytic activity of WO$_3$ NR arrays deposited in various growth times (**Figure 7e**).[23]

7

Initially, photocatalytic activity increased with NR growth time from 30s, reaching a maximum at a growth time of 5 mins. From this point, the photocatalytic activity decreased with increasing growth time. Therefore the trend in photocatalytic activity reflected the two regimes of electronic structure and defect chemistry described above. The samples with short growth times exhibiting quantum confinement and fully oxidised tungsten cations, showed photocatalytic activity that increased with deposition time. The most photocatalytic active sample was the sample grown for 5 mins (FQE = 8.7 ± 0.4 x 10^{-5} molecules per photon, much higher than a commercially available self-cleaning coating, Pilkington Activ[TM] glass, with FQE = 0.7 x 10^{-5} molecules per photon under irradiation by UVA at 365 nm,[24] is used for reference), which contained a small amount of reduced tungsten states but still possessed a bandgap significantly wider than bulk WO_3, *i.e.* VB is at a more positive potential, giving rise to greater oxidation over-potential compared to bulk WO_3. At longer deposition times the bandgap decreased, which might be expected to improve photocatalytic performance as the material will absorb more of the incident light. However the photocatalytic activity decreased, which correlates with the presence of the reduced tungsten states (V_O). The presence of V_O can cause charge carriers to be strongly localized, and hence inhibit their movement to the material surface where they can react.[25,26] Consequently the photocatalytic performance of our WO_3 NRs decreased with an increase in V_O, found in samples with growth times greater than 5 minutes.

3. Conclusions

The photocatalytic performance of nanostructured tungsten oxide, grown by chemical vapour deposition, can be correlated to changes in the electronic band structure as well as the presence of oxygen vacancies. The results indicate that for maximum photocatalytic performance for organic pollutant degradation, tungsten oxide should be engineered so that the bandgap is widened relative to bulk WO_3 to a value above 3 eV; although less visible light

would be absorbed in this region, increases in the over-potential for oxidation reactions offset this loss. It is also desirable to ensure the material remains defect free, or the defect concentration is minimised, to minimise carrier recombination. This study can be used a general guide for defect engineering.[27,28]

4. Experimental Section

Synthesis of WO₃ NR arrays: Tungsten oxide NR arrays were prepared by AACVD, a solution-based variant of conventional chemical vapour deposition CVD which we have previously demonstrated for the controlled growth of nanostructured tungsten oxide.[12,29] The precursor solution of $W(CO)_6$ (99%, Aldrich) dissolved in 2:1 a mixture of acetone (99%, Emplura) and methanol (99.5%, Emplura) (1.37×10^{-2} M) was used to generate aerosols by an ultrasonic humidifier (Liquifog, Johnson Matthey operating at 2 MHz) transported to the reactor using nitrogen carrier gas (99.99%, BOC, flow rate 300 sccm) controlled by a mass flow controller (MFC, Brooks), and then deposited on a quartz substrate at set-temperature (375 °C) for 0.5 to 30 min, After deposition the heater and humidifier were switched off to stop deposition and the reactor naturally cooled under N_2 to room temperature. The inlet to the cold wall reactor of the AACVD system is equipped with a water jacket to avoid precursor overheating and decomposition prior to entering the reactor chamber and the exhaust was directly vented into the extraction system of the fume cupboard. Finally, the as-synthesized thin films were put into furnace for annealing at 500 °C in air for 2 hour (Schematic outline of AACVD process shown in **Figure S1**).[12]

Characterization: Scanning Electron Microscopy (SEM) images were obtained on a JEOL 6301F. Samples were coated with gold for 60 seconds and scanned at 5 kV. X-Ray diffraction (XRD) patterns were acquired on a Bruker D8-Discover reflection diffractometer equipped with a LinxEye silicon strip detector using Cu Kα radiation operated at 40 kV and 40 mA.The X-ray photoelectron (XPS) analysis was carried out on a Thermo Scientific K-

Alpha instrument equipped with a monochromatic Al Kα radiation (1486.6 eV) with charge compensation by a beam charge neutralization argon-ion gun (≤ 10 eV), and calibrated by the C 1s peak at 284.8 eV. Peak fitting was carried out by using "CasaXPS software (Version 2.3.16)".[30,31] Transmission electron microscopy (TEM) and scanning TEM (STEM) analysis was performed on a JEOL 2100 at 300 KV equipped with energy dispersion X-ray (EDX) detector (X-MaxN 80, Oxford Instruments). UV/vis spectroscopy was performed using a double monochromated PerkinElmer Lambda 950 UV/vis/NIR spectrophotometer in the 250−2500 nm range recording the transmittance % and reflectance % of tungsten oxide NR arrays on quartz. The absorbance % is estimated by:

$$A\% = 100\% - (T\% + R\%) \quad (1)$$

where A, T and R are absorbance, transmittance and reflectance respectively.

Finally, the band gap of tungsten oxide NR arrays is determined with the following equation:

$$\alpha = A\left[\left(h\nu - E_g\right)^{n/2}/h\nu\right] \quad (2)$$

where α, A, E_g, ν and n are the absorption coefficient, constant, band gap, incident light frequency and an integer respectively, whilst the value of integer n depends on the characteristics of the optical transition (n = 1 or 4 for direct or indirect band transition respectively).[32] The indirect bandgap of all samples were obtained for the plot of $(\alpha h\nu)^{1/2}$ vs. $h\nu$.

Photocatalytic activity tests: the as-synthesized WO$_3$ thin films were dip-coated with a thin layer of SA from a 0.05 M SA and chloroform solution, and then irradiated by UVA bulb (Philips TL-D 18W BLB*4) (4.2 mW cm^{-2}) in spectra range of 340 to 410 nm (maximum at 365 nm)[33] (**Figure 8**) with area of samples 0.78 cm^2. One of the great advantages of using

stearic acid to assess the photocatalytic efficiency of semiconductor photocatalysts is the fact that stearic acid is a very stable organic pollutant under UV irradiation in the absence of a photocatalyst host. The photodegradation of SA was monitored by a Fourier transform infrared (FTIR) spectrometer (Perkin Elmer RX-1) in the range from 2700-3000 cm^{-1}. The overall SA degradation reaction is:

$$CH_3(CH_2)_{16}CO_2 \longrightarrow 18CO_2 + 18H_2O \quad (3)$$
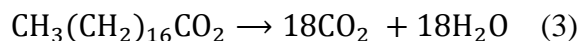
To evaluate the activity of photodegradation of SA, the IR spectra were collected in absorbance mode and the areas of typical peaks (at 2958, 2923 and 2853 cm^{-1} representing C-H bonds of SA), integrated to give an estimation of the number of SA molecules degraded during irradiated by UV light using a conversion factor (1 cm^{-1} $\equiv$ 9.7×10^{15} molecules) presented in the literature.[34] The photodegraduation rate of SA (zero order kinetics) were estimated from linear regression of the initial 40 to 50 % degradation steps, and then given a formal quantum efficiency (FQE) values defining the number of SA molecules photodegraded by per incident photon (365 nm). The FQE can be calculated by:[35]

$$FQE = \frac{|d[SA]/dt|}{d[h\nu]_{inc}/dt} \quad (4)$$

where $d[SA]/dt$ is the rate of removal of SA (molecules per second, estimated by integrated area of IR spectra peaks times the conversion factor), and $d[h\nu]_{inc}/dt$ is the rate of incident light (photons per second) assuming all incident photons absorbed had the same energy 3.4 eV (365 nm).

Supporting Information
Supporting Information of additional SEM images, XPS valence band spectra and FT-IR spectra is available from the Wiley Online Library.

Received: ((will be filled in by the editorial staff))
Revised: ((will be filled in by the editorial staff))
Published online: ((will be filled in by the editorial staff))

References

[1]   A. Kudo, Y. Miseki, *Chem. Soc. Rev.* **2009**, *38*, 253.

[2]   A. Mills, S. Le Hunte, *J. Photochem. Photobiol. A Chem.* **1997**, *108*, 1.

[3]   A. Mills, R. H. Davies, D. Worsley, *Chem. Soc. Rev.* **1993**, *22*, 417.

[4]   R. Quesada-Cabrera, C. Sotelo-Vazquez, J. A. Darr, I. P. Parkin, *Appl. Catal. B Environ.* **2014**, *160–161*, 582.

[5]   M. G. Walter, E. L. Warren, J. R. McKone, S. W. Boettcher, Q. Mi, E. A. Santori, N. S. Lewis, *Chem. Rev.* **2011**, *111*, 5815.

[6]   A. Walsh, J. L. F. Da Silva, S.-H. Wei, C. Körber, A. Klein, L. F. J. Piper, A. DeMasi, K. E. Smith, G. Panaccione, P. Torelli, D. J. Payne, A. Bourlange, R. G. Egdell, *Phys. Rev. Lett.* **2008**, *100*, 167402.

[7]   W. L. Ng, M. A. Lourenço, R. M. Gwilliam, S. Ledain, G. Shao, K. P. Homewood, *Nature* **2001**, *410*, 192.

[8]   H. Watanabe, K. Fujikata, Y. Oaki, H. Imai, *Chem. Commun. (Camb).* **2013**, *49*, 8477.

[9]   Y. H. Hu, *Angew. Chem. Int. Ed. Engl.* **2012**, *51*, 12410.

[10]   A. Naldoni, M. Allieta, S. Santangelo, M. Marelli, F. Fabbri, S. Cappelli, C. L. Bianchi, R. Psaro, V. Dal Santo, *J. Am. Chem. Soc.* **2012**, *134*, 7600.

[11]   Y. Li, Z. Tang, J. Zhang, Z. Zhang, *J. Phys. Chem. C* **2016**, *120*, 9750.

[12]   M. Ling, C. Blackman, *Phys. status solidi* **2015**, *12*, 869.

[13]   A. M. Smith, M. G. Kast, B. A. Nail, S. Aloni, S. W. Boettcher, *J. Mater. Chem. A* **2014**, *2*, 6121.

[14]   J. Zhou, Y. Ding, S. Z. Deng, L. Gong, N. S. Xu, Z. L. Wang, *Adv. Mater.* **2005**, *17*,

2107.

[15] Q. Sun, B. K. Rao, P. Jena, D. Stolcic, Y. D. Kim, G. Gantefor, A. W. Castleman, *J. Chem. Phys.* **2004**, *121*, 9417.

[16] C. A. Triana, C. G. Granqvist, G. A. Niklasson, *J. Appl. Phys.* **2015**, *118*, 24901.

[17] F. Wang, C. Di Valentin, G. Pacchioni, *Phys. Rev. B* **2011**, *84*, 73103.

[18] A. Larsson, *Solid State Ionics* **2003**, *165*, 35.

[19] M. B. Johansson, B. Zietz, G. A. Niklasson, L. Österlund, *J. Appl. Phys.* **2014**, *115*, 213510.

[20] H. LIN, C. HUANG, W. LI, C. NI, S. SHAH, Y. TSENG, *Appl. Catal. B Environ.* **2006**, *68*, 1.

[21] M. T. Greiner, M. G. Helander, W.-M. Tang, Z.-B. Wang, J. Qiu, Z.-H. Lu, *Nat. Mater.* **2012**, *11*, 76.

[22] M. M. Y. A. Alsaif, A. F. Chrimes, T. Daeneke, S. Balendhran, D. O. Bellisario, Y. Son, M. R. Field, W. Zhang, H. Nili, E. P. Nguyen, K. Latham, J. van Embden, M. S. Strano, J. Z. Ou, K. Kalantar-zadeh, *Adv. Funct. Mater.* **2016**, *26*, 91.

[23] R. Quesada-Cabrera, C. Sotelo-Vazquez, J. C. Bear, J. A. Darr, I. P. Parkin, *Adv. Mater. Interfaces* **2014**, *1*, 1.

[24] A. Mills, A. Lepre, N. Elliott, S. Bhopal, I. P. Parkin, S. A. O'Neill, *J. Photochem. Photobiol. A Chem.* **2003**, *160*, 213.

[25] A. J. E. Rettie, W. D. Chemelewski, D. Emin, C. B. Mullins, *J. Phys. Chem. Lett.* **2016**, *7*, 471.

[26] K. P. H. M. A. Lourenço, M. S. A. Siddiqui, G. Shao, R. M. Gwilliam, in *Towar. First Silicon Laser*, Springer Netherlands, **2003**, pp. 11–20.

[27] H. L. Tuller, S. R. Bishop, *Annu. Rev. Mater. Res.* **2011**, *41*, 369.

[28] E. L. Runnerstrom, A. Bergerud, A. Agrawal, R. W. Johns, C. J. Dahlman, A. Singh, S. M. Selbach, D. J. Milliron, *Nano Lett.* **2016**, *16*, 3390.

[29]   P. Marchand, I. A. Hassan, I. P. Parkin, C. J. Carmalt, *Dalton Trans.* **2013**, *42*, 9406.

[30]   S. F. Ho, S. Contarini, J. W. Rabalais, *J. Phys. Chem.* **1987**, *91*, 4779.

[31]   P. Biloen, G. T. Pott, *J. Catal.* **1973**, *30*, 169.

[32]   D. Chen, J. Ye, *Adv. Funct. Mater.* **2008**, *18*, 1922.

[33]   K. Philips, "Product information TL-D Blacklight Blue," can be found under

http://www.lighting.philips.co.uk/prof/lamps/fluorescent-lamps-and-starters/tl-d/tl-d-

blacklight-blue/928048010805_EU/product, **2015**.

[34]   A. Mills, J. Wang, *J. Photochem. Photobiol. A Chem.* **2006**, *182*, 181.

[35]   J. M. Buriak, P. V. Kamat, K. S. Schanze, *ACS Appl. Mater. Interfaces* **2014**, *6*, 11815.
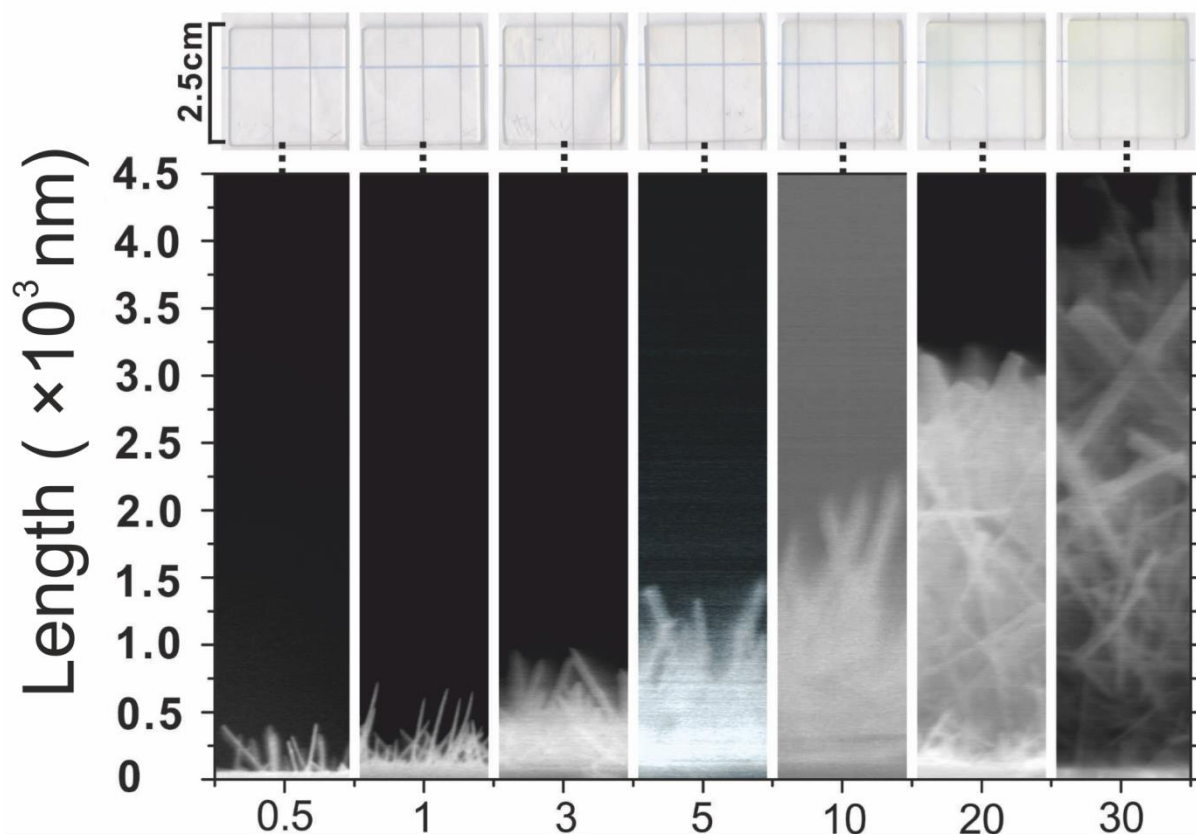
Figure 1. Photographs of WO_3 thin films (2.5 × 2.5 cm) grown for 0.5, 1, 3, 5, 10, 20 and 30 minutes (from left to right) *via* AACVD (top) which result in a change in length of the NRs from around 400 to 4500 nm (images of cross-section SEM, middle).
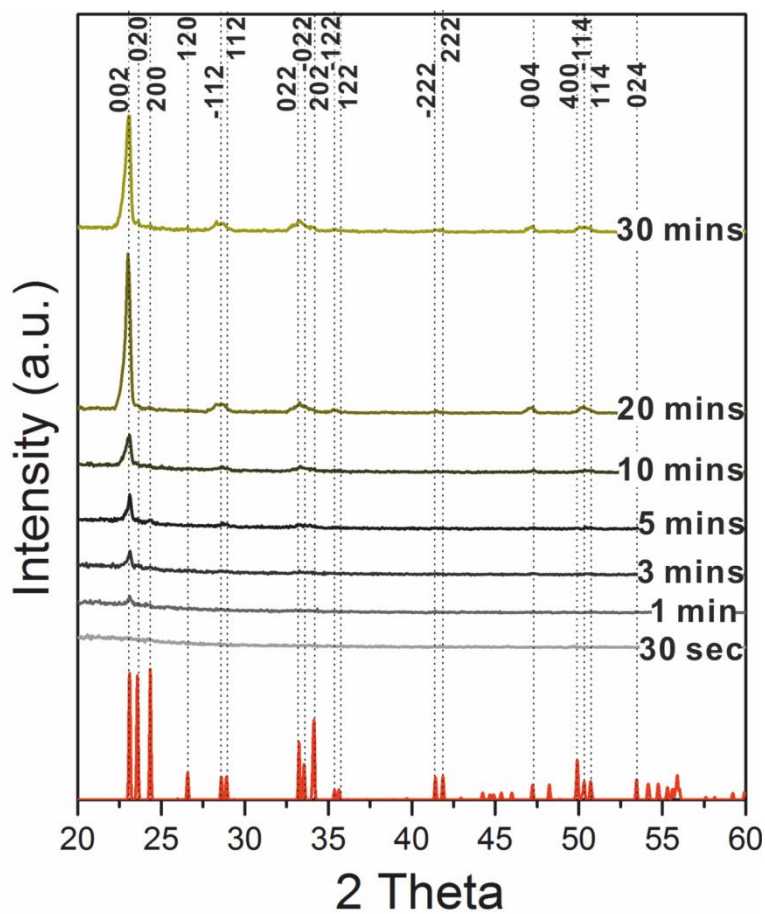
Figure 2. Glancing angle XRD patterns of the WO$_3$ thin films, with growth time shown on the right, all conforming to the monoclinic WO$_3$ crystal structure (PDF# 01-072-0677) shown in red.
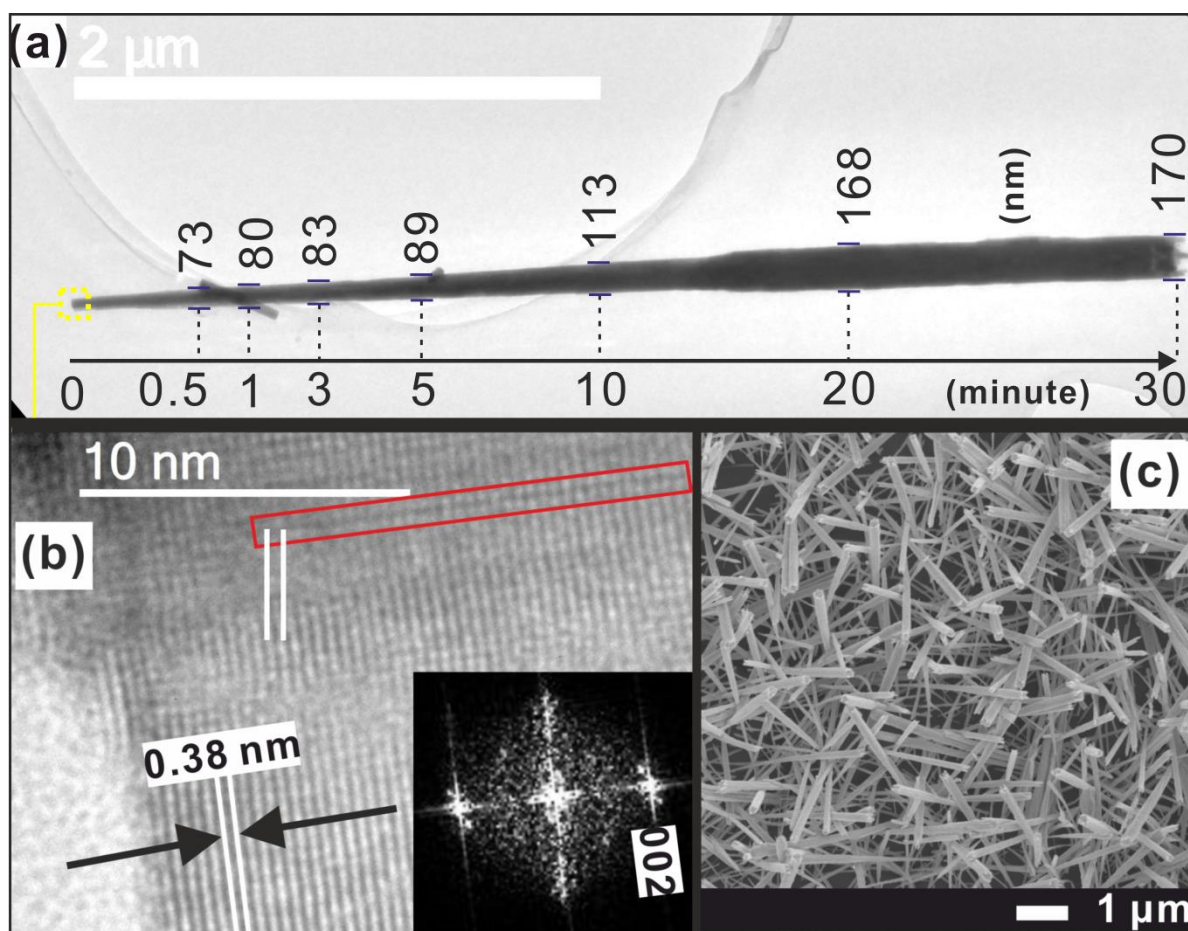
Figure 3. (a) A typical TEM image of a single NR from a sample deposited for 30 mins, correlating the width of the NR observed at a particular growth time with the distance along the abstracted nanorod length (measurements were taken based on the varying NR length obtained from samples grown for 0.5 to 30 mins shown in Figure 1). (b) a HRTEM image showing how the interplanar spacing 0.38 (± 0.01) nm correponds to preferred growth in the [002] plane, with planar defects (red rectangle) that form parallel to the growth direction. (c) a top down SEM image of the NR array.
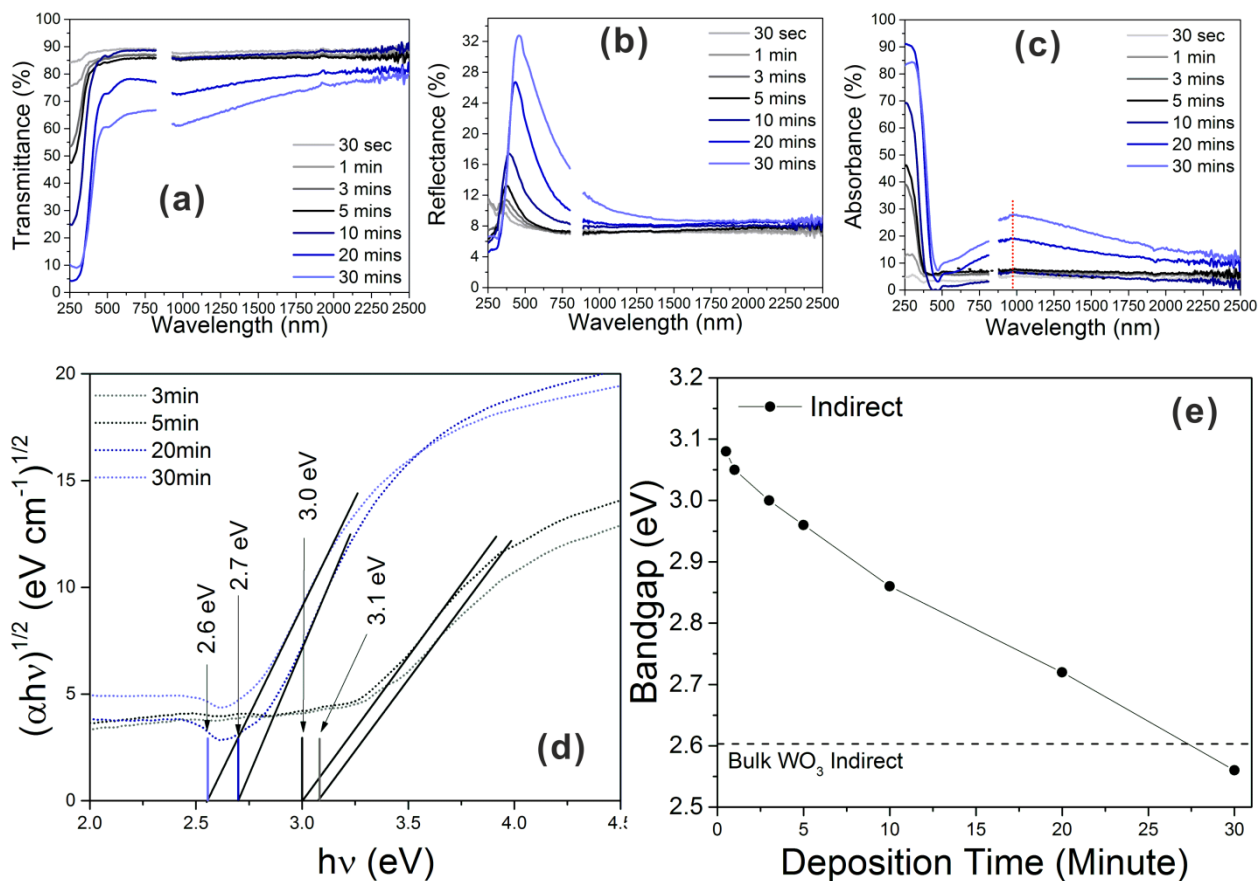
Figure 4. The (a) transmittance, (b) reflectance and (c) absorbance spectra of WO₃ NR arrays deposited on quartz with growth times from 0.5 to 30 mins (aberrant data due to a grating change in the UV-Vis spectrometer has been removed). (d) Absorption data was used to calculate the indirect bandgap E_g from Tauc plots (more in **Figure S4**). (e) The change in indirect bandgap E_g with deposition time (0.5 to 30 min) shown alongside the indirect bandgap E_g of bulk WO₃ (2.62 eV, dotted line).[15]
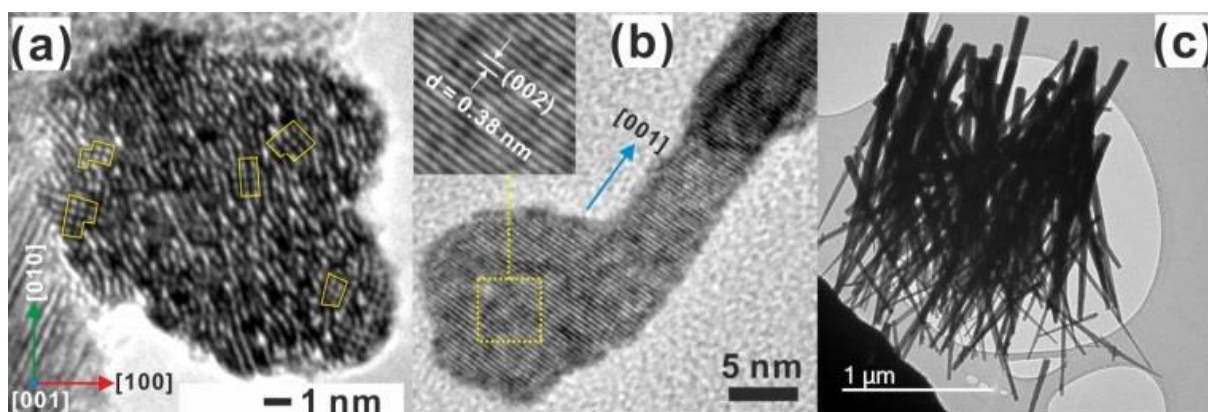

Figure 5. (a) HRTEM of a WO₃ growth site showing dislocation loops (yellow circle) in the [010] and [100] directions of diameter ~ 0.4 to 1.5 nm. (b) A NR extruding from a growth site and growth along direction [001]. (c) TEM image of the NR array.
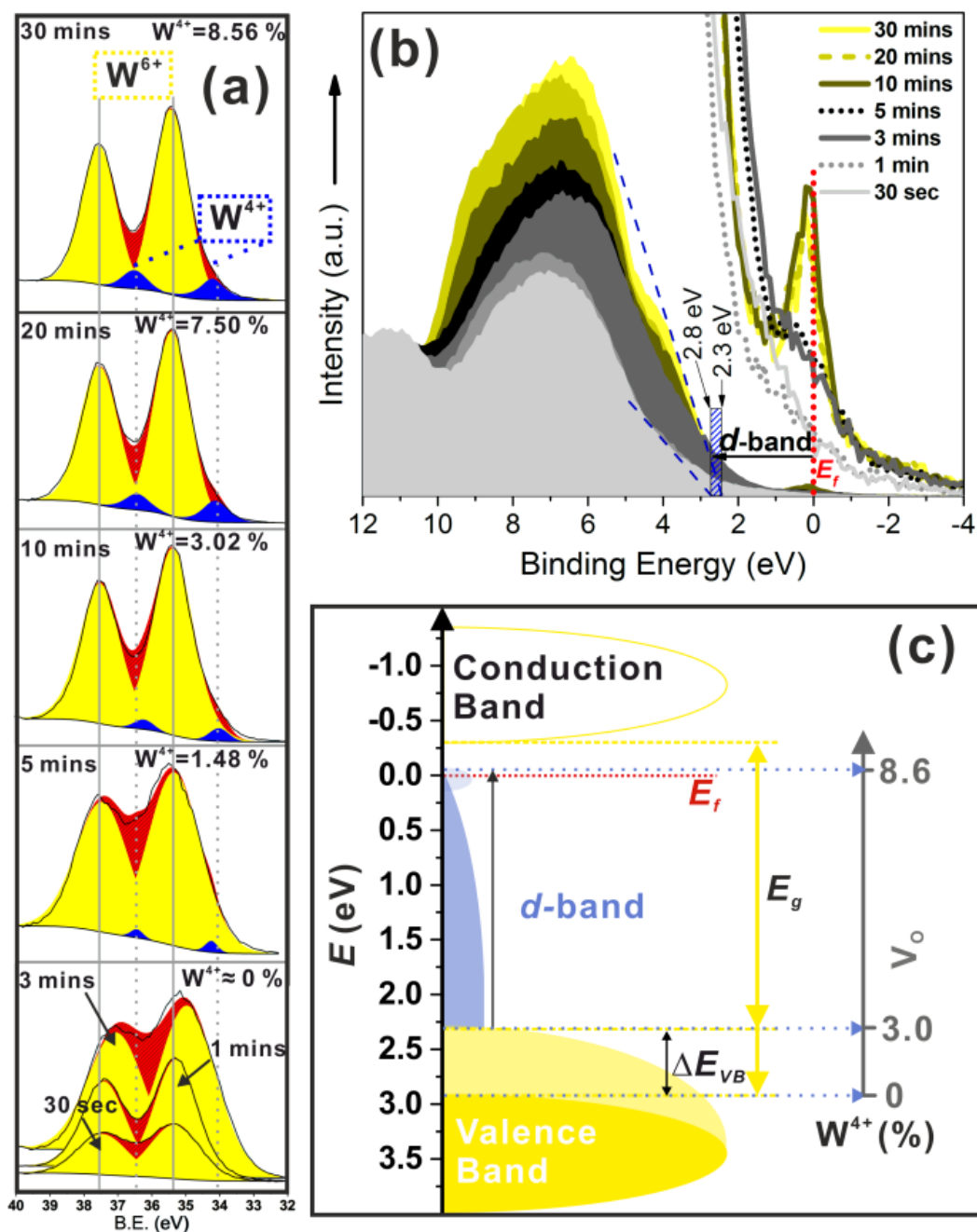
Figure 6. XPS spectra for the (a) W 4f region, (b) valance band and (c) schematic band structure of WO_3 NR arrays grown for between 0.5 and 30 mins [calibrated to graphitic carbon 1s = 284.8 eV and the respective Fermi level (E_f = 0 eV). (c) The expansion of d-band of W^{4+} and E_g with red shift of VB is dependent on the increase of W^{4+} (from 0 to 8.6 %) attributed to an increase in oxygen vacancies (V_O).
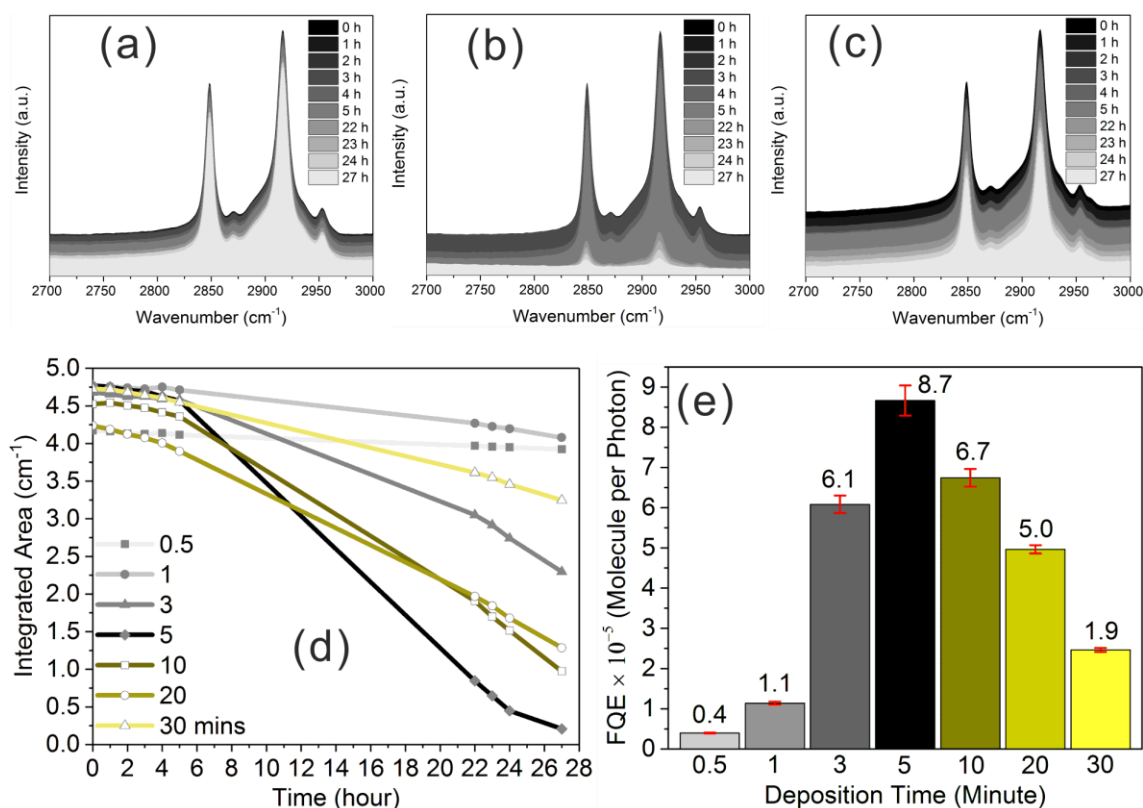
Figure 7. Infrared spectra showing the photodegradation of stearic acid (SA) upon UVA irradiation (4.2 mW cm^{-2}) on a range of WO$_3$ NR arrays of various growth times of (a) 0.5 min, (b) 5 min, (c) 30 min (1, 3, 10 and 20 min in Figure S6), where a decrease is caused by photocatalytic oxidation. (d) Integrated areas of the peaks of the C-H stretches of stearic acid (a to c and Figure S6) illuminating by UVA from 0 to 27 hour. (e) Photocatalytic activity for the photodegradation of stearic acid are quoted in terms of formal quantum efficiency (FQE), which corresponds to the number of SA molecules degraded per incident photon, calculated from the initial rates of photodegradation.
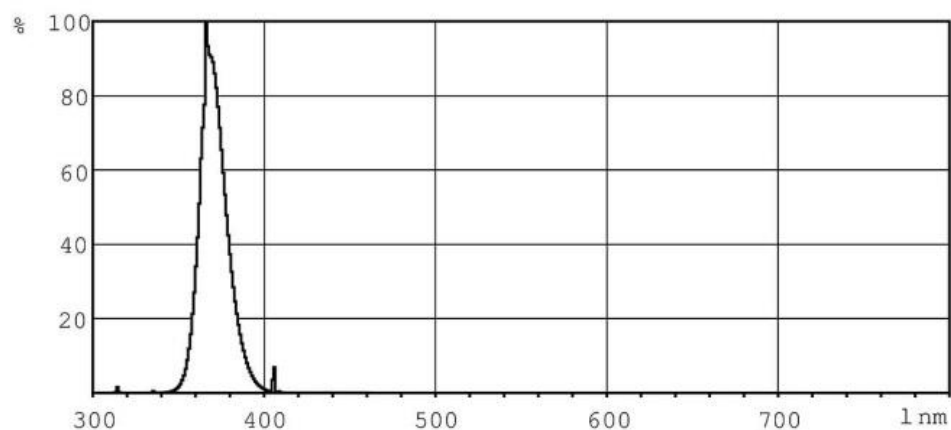

Figure 8. Spectra of UVA light (Philips, TL-D 18W BLB).[33]

Table 1. A summary of the XPS results, which relate changes in indirect bandgap, concentration (at. %) of W^{4+}, VBM position and the peak maxima of NIR absorption with deposition time.

Depos. time	Indirect Bandgap	W^{4+}	VBM	NIR absorption peak
(minute)	(eV)	(at. %)	(eV)	(nm)
30	2.6	8.56	2.32	986
20	2.7	7.50	2.37	970
10	2.9	3.02	2.41	968
5	3.0	1.48	2.65	n/a
3	3.0	trace	2.67	n/a
1	3.1	trace	2.72	n/a
0.5	3.1	trace	2.78	n/a

The table of contents entry should be 50–60 words long, and the first phrase should be bold.

The electronic structure, defect chemistry, optical bandgap and photocatalytic activity were found to vary progressively with nanorod length and width of Tungsten trioxide nanorod arrays deposited using aerosol assisted chemical vapour deposition.

Min Ling, Christopher S. Blackman,[*] Robert G. Palgrave, Carlos Sotelo-Vazquez, Andreas Kafizas and Ivan P. Parkin

Correlation of Optical Properties, Electronic Structure and Photocatalytic Activity in Nanostructured Tungsten Oxide

ToC figure ((Please choose one size: 55 mm broad × 50 mm high **or** 110 mm broad × 20 mm high. Please do not use any other dimensions))
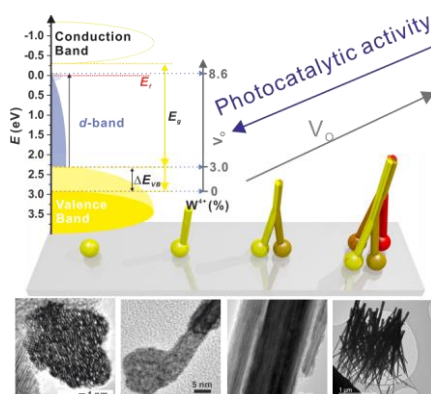
Supporting Information

Correlation of Optical Properties, Electronic Structure and Photocatalytic Activity in Nanostructured Tungsten Oxide

Min Ling, Christopher S. Blackman,[*] Robert G. Palgrave, Carlos Sotelo-Vazquez, Andreas Kafizas and Ivan P. Parkin
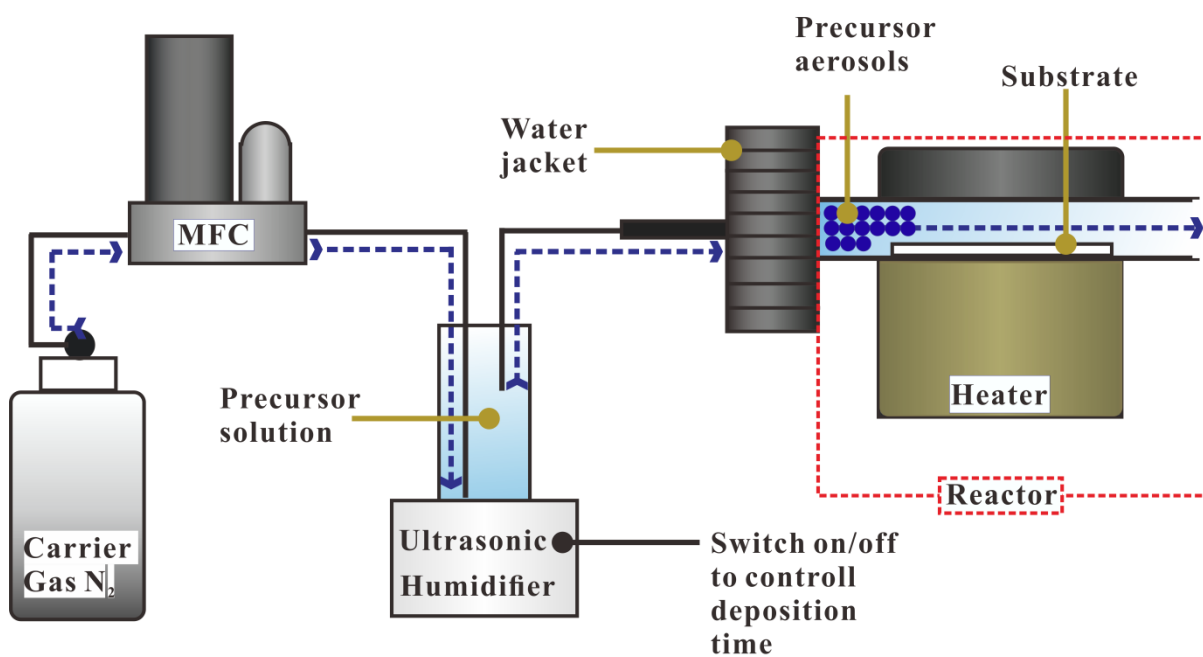
1. **Experimental**

Figure S 1. Schematic flow diagram of the AACVD process.
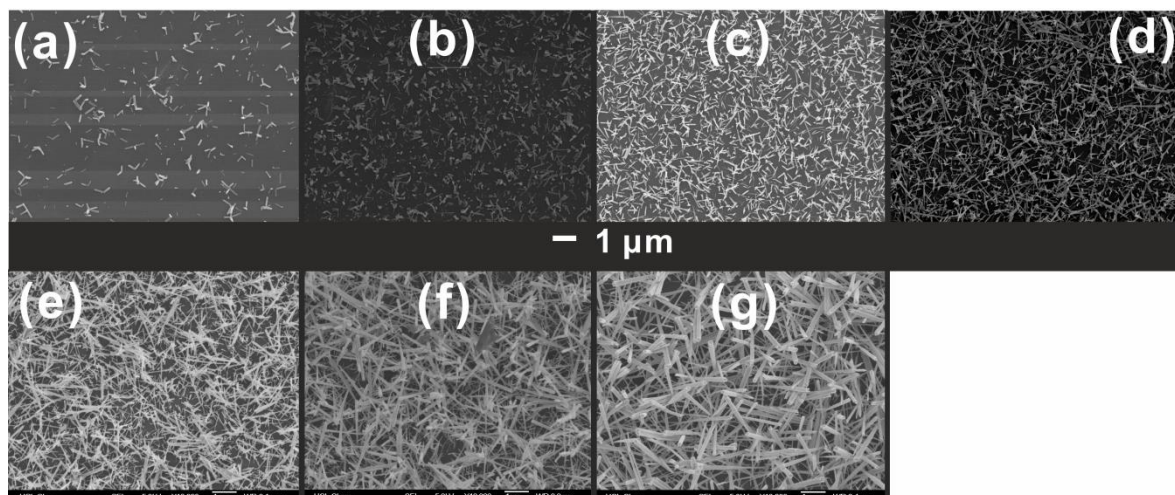
2. **Results**

Figure S 2. SEM images of WO$_3$ thin fims depostied in 0.5 (a), 1(b), 3(c), 5(d), 10(e), 20(f)fand 30 minutes (g) via AACVD.
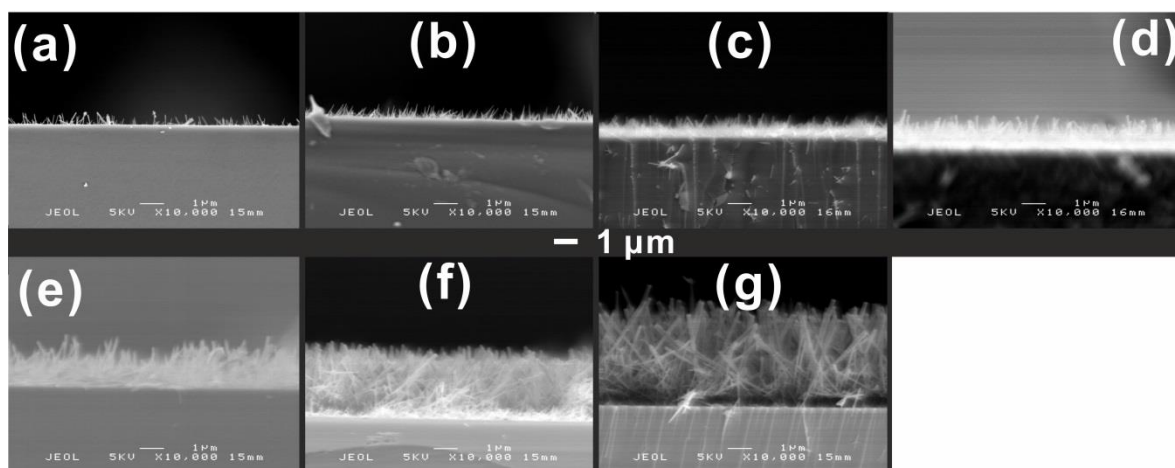

Figure S 3. Cross-section SEM images of WO$_3$ thin fims depostied in 0.5 (a), 1(b), 3(c), 5(d), 10(e), 20(f)fand 30 minutes (g) via AACVD.
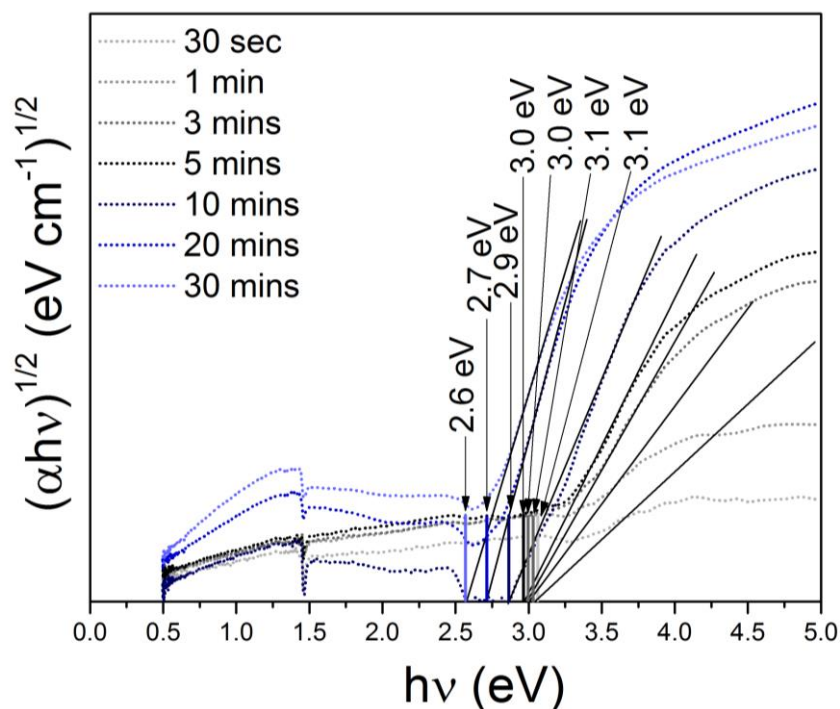
Figure S 4. Absorption data (Figure 2c) was used to calculate the indirect bandgap E_g of WO$_3$ NR array thin films deposited for 0.5 to 30 min from Tauc plots.
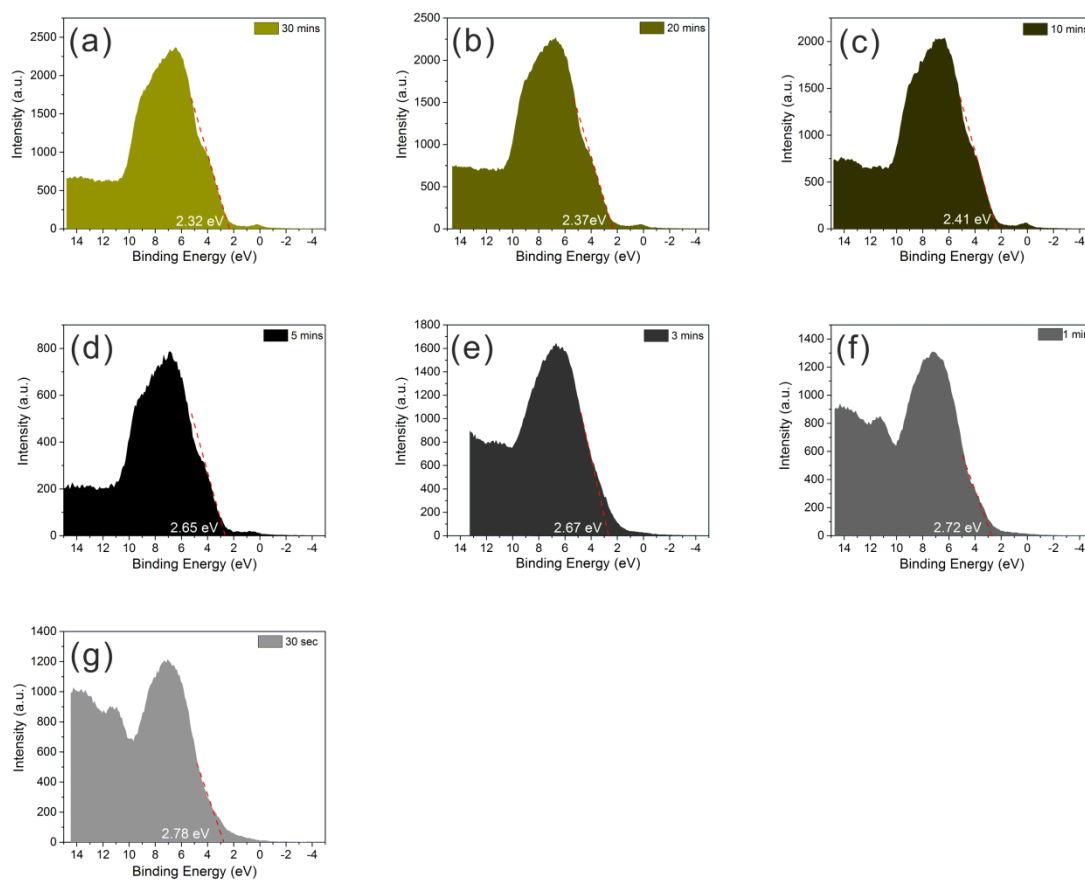

Figure S 5. XPS spectra for the valance band of WO$_3$ thin films with NRs strucutre deposited on quartz after 30 mins to 30 seconds (a to g) with reference C1s peak calibrated to 284.8 eV.
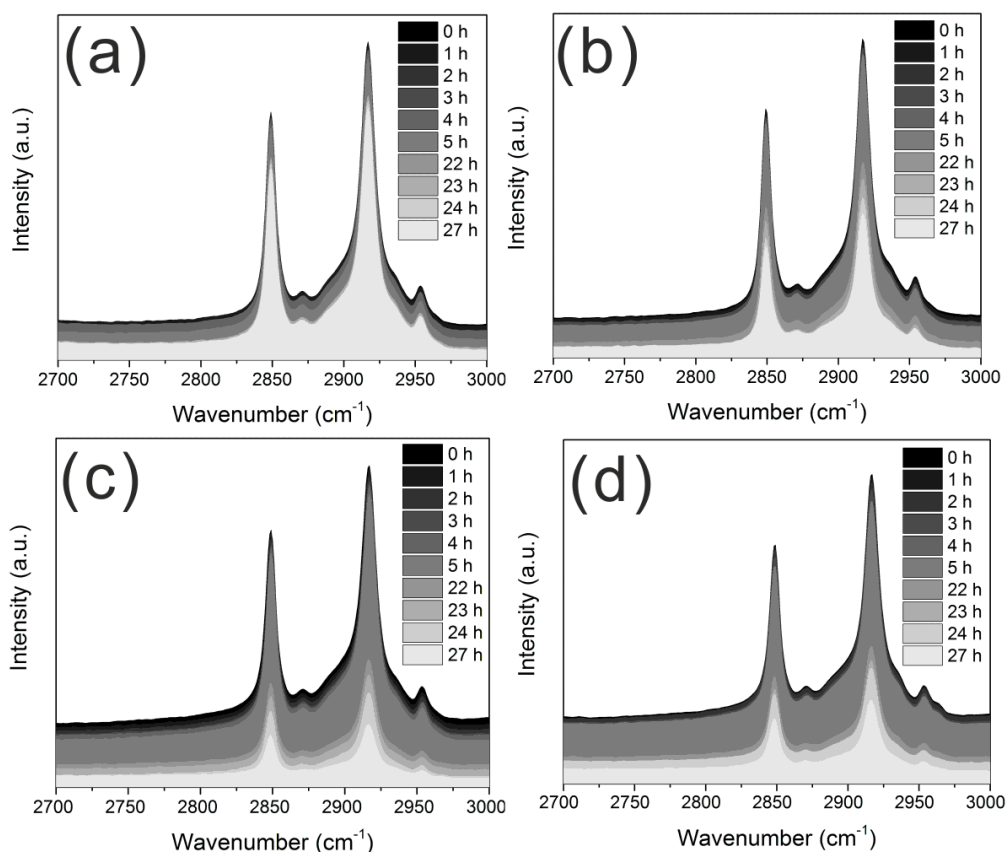
Figure S 6. Infrared spectra showing the photodegradation of stearic acid (SA) upon UVA irradiation (4.2 mW cm^{-2}) on a range of WO$_3$ NR arrays of various growth times of (a) 1 min, (b) 2 min, (c) 10 min and (d) 20 min.

	A	B	C	D	E1	E2	E3	E4	E5
1	Equation	y = a + b*x							
2	Weight	No Weighting							
3	Residual Sum of Squares	4.80087E-4	0.00752	0.21445	0.42353	0.21445	0.04805	0.01248	0.00298
4	Pearson's r	-0.99736	-0.99496	-0.99496	-0.99351	-0.99496	-0.9983	-0.9982	-0.93082
5	Adj. R-Square	0.99407	0.98869	0.9887	0.98522	0.9887	0.99617	0.99596	0.84973
6			Value	Standard Error					
7		Intercept	4.16282	0.00353					
8		Slope	-0.00891	2.29346E-4	30 s				
9		Intercept	4.80465	0.01398					
10		Slope	-0.02547	9.07561E-4	1 min				
11		Intercept	4.80127	0.07467					
12		Slope	-0.1361	0.00485	3 min				
13		Intercept	5.15036	0.11336					
14	Integrated Area	Slope	-0.1939	0.00839	5 min				
15		Intercept	4.80127	0.07467					
16		Slope	-0.1361	0.00485	10min				
17		Intercept	4.3623	0.03535					
18		Slope	-0.11101	0.00229	20min				
19		Intercept	4.78917	0.01801					
20		Slope	-0.0551	0.00117	30min				
21		--	--	--	--				
22		--	--	--	--				

Figure S 7. Results of linear regression of initial (40 to 50 %) step of integrated area of obtained IR spectra peak at 2958, 2923 and 2853 cm^{-1} dependent on the UVA illumination time from 0 to 27 hour (Figure 6d).